Early science with Korean VLBI network: evaluation of system performance

Sang-Sung Lee[1], Leonid Petrov[2], Do-Young Byun[1], Jongsoo Kim[1], Taehyun Jung[1], Min-Gyu Song[1], Chung Sik Oh[1], Duk-Gyoo Roh[1], Do-Heung Je[1], Seog-Oh Wi[1], Bong Won Sohn[1], Se-Jin Oh[1], Kee-Tae Kim[1], Jae-Hwan Yeom[1], Moon-Hee Chung[1], Jiman Kang[1], Seog-Tae Han[1], Jung-Won Lee[1], Bong Gyu Kim[1], Hyunsoo Chung[1], Hyun-Goo Kim[1], Hyo Ryoung Kim[1], Yong-Woo Kang[1], and Se-Hyung Cho[1]

ABSTRACT

We report VLBI observing performance of the Korean VLBI Network (KVN). The KVN is the first millimeter-dedicated VLBI network in East Asia. The KVN consists of three 21-m radio telescopes with the baseline lengths in a range of 305–476 km. The quasi-optical system equipped on the antennas allows simultaneous observations at 22, 43, 86, and 129 GHz. The first fringes of KVN were obtained at 22 GHz on 2010 June 8. Test observations at 22 and 43 GHz on 2010 September 30 and 2011 April 4 confirmed that the full cycle of VLBI observations works according to specification: scheduling, antenna control system, data recording, correlation, post-correlation data processing, astrometry, geodesy, and imaging analysis. We found decorrelation due to instability in the hardware at times up to 600 s is negligible. The atmosphere fluctuations at KVN baseline are partly coherent, which allows us to extend integration time under good winter weather conditions up to 600 s without significant loss of coherence. The postfit residuals at KVN baselines do not exhibit systematic patterns, and the weighted root mean square (wrms) of residuals is 14.8 ps. KVN is ready for imaging compact radio sources both in snapshot and full-track modes with residual noise in calibrated phases less than 2 degrees at 22 and 43 GHz and with dynamic ranges of 300 for snapshot mode and 1000 for full-track mode. With simultaneous multi-frequency observations, KVN can be used to make parsec-scale spectral-index maps of compact radio sources.

Subject headings: astronomical instrumentation - instrumentation: interferometers - techniques: interferometric - telescopes

1. Introduction

The Korean VLBI Network (KVN) is a three-element Very Long Baseline Interferometry (VLBI) network in Korea, which is dedicated to VLBI observations at millimeter wavelengths. Three 21-m radio telescopes are located in Seoul, Ulsan and Jeju island, Korea; KVN Yonsei Radio Observatory (KY), KVN Ulsan Radio Observatory (KU), and KVN Tanma Radio Observatory (KT) (Figure1). The baseline lengths are in a range of 305–476 km. All antennas have the identical design. The antennas are equipped with the quasi-optical system that allows simultaneous observations at 22, 43, 86, and 129 GHz. This system is described in detail in Han et al. (2008, 2013).

The KVN was built by Korea Astronomy and Space Science Institute (KASI) for achieving the main goals; a)to study the formation and death of stars with observing water (H2O), methanol (CH3OH), and silicon monoxide (SiO) masers at high resolutions, b)to investigate the structure and dynamics of our own Galaxy by conduct-

[1] Korea Astronomy and Space Science Institute, Daedeokdae-ro 76, Yuseong, Daejeon 305-348, Republic of Korea;sslee@kasi.re.kr

[2]Astrogeo Center, Falls Church, VA 22043, USA

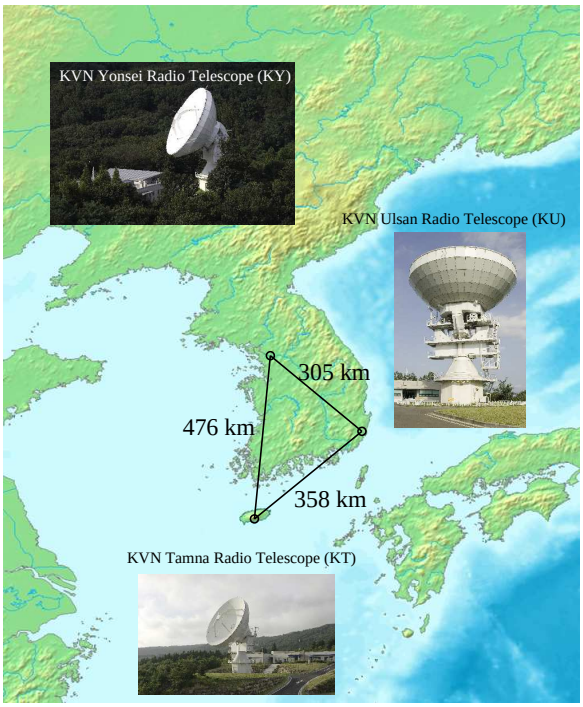

Fig. 1.— The Korean VLBI Network.

ing highly accurate astrometric VLBI observations toward the galactic radio sources, and c)to study the nature of active galactic nuclei (AGN) and their population at high frequencies. The KVN as a dedicated-VLBI network also aims to study the spectral and temporal properties of transient sources such as bursting star-forming regions, intra-day variable compact radio sources, gamma-ray flaring AGNs, etc by conducting systematic multi-wavelength monitoring campaigns (Kim et al. 2004; Lee et al. 2011).

Singe dish performance of the KVN 21-m radio telescopes was tested at 22 and 43 GHz in 2008-2011 and then at 86 and 129 GHz in 2012. Based on the performance tests, we confirmed that the telescopes are suitable for simultaneous multi-frequency single polarization observations at 22, 43, 86 and 129 GHz (Lee et al. 2011; Han et al. 2013). The dual beams at 22 and 43 GHz are well aligned within 5 arcseconds. The pointing accuracies are <3 arcseconds in azimuth and elevation, respectively. The measured aperture efficiencies are of $> 64\%$ at 22 GHz and $> 62\%$ at 43 GHz, the main-beam efficiencies are $> 49\%$ at 22 GHz and $> 50\%$ at 43 GHz, and the efficiencies derived from observations of the Moon, assuming its brightness temperature 225 K (Linsky 1973; Mangum 1993), are $> 77\%$ at 22 GHz and $> 85\%$ at 43 GHz. The elevation dependence of the aperture efficiencies is less than 5% at higher elevations than $> 20°$, which is negligible. Unique receiving systems, accurate beam alignment, and high antenna efficiencies will provide us with good opportunities both for single-dish and VLBI observations at millimeter wavelengths.

The KASI has all hardware and software to support *the full cycle of VLBI observations* either as a three-element interferometer or as a part of a larger VLBI network: scheduling, antenna control system, data recording, correlation, post-correlation data processing, astrometry, geodesy, and imaging analysis. The first fringes of KVN were obtained at 22 GHz on 2010 June 8. The data were recorded at a recording rate of 1 Gbps.

In collaboration with the VLBI Exploration of Radio Astrometry (VERA), performance of combined VLBI network between KVN and VERA at 22 and 43 GHz was tested since 2008 using K4 terminal at a recording rate of 128 Mbps. Results of the tests will be described in separate papers.

In this paper we present results of the VLBI test observations with the KVN on 2010 September 30 at 22 GHz and on 2011 April 4 at 22 and 43 GHz. We describe the VLBI system of KVN, the strategy of observations, data analysis and present the evaluation results of KVN. Finally, we summarize what we found about the VLBI performance of KVN.

2. VLBI system

All KVN antennas are identically designed (Kim et al. 2011). Specification of the antennas, optics, receiving systems, etc, are described in Lee et al. (2011). In this section, we focus on introducing VLBI-related systems for KVN such as antenna sites, array, sensitivities, clock system, recording system and correlators.

2.1. Antenna sites

Table 1 gives the geographic locations of three KVN antennas, which were measured with GPS systems. Statistical uncertainty of position of the GPS antenna reference points is several centimeters. However the vector between the radio tele-

cope reference points and the GPS antenna reference points was known with accuracy of several decimeters. Future geodetic VLBI observations will allow to determine position of radio telescope reference points with millimeter accuracy.

The KVN antennas are controlled remotely from the Array Operation Center (AOC) at the KASI headquarter in Daejeon, Korea. The KVN stations are connected with the AOC through high speed dedicated network, KREONET (Korea Research Environment Open NETwork). The high speed network is also used for quick fringe tests of KVN internal baselines and for international e-VLBI tests with European VLBI Network (EVN) and Long Baseline Array (LBA). The real-time KVN-EVN and KVN-LBA fringes at 22 GHz were successfully obtained **first time in 2011 October at the Joint Institute for VLBI in Europe (JIVE), the Netherlands and in 2012 March at Curtin University in Perth, Australia.**

Corr 1

Since the KVN antennas are operated remotely from the AOC, it is necessary for the AOC operator to know the weather conditions which could influence the VLBI data quality during observations. There is a weather station at each KVN observatory sending information on the air temperature, dew point, wind speed, wind direction and air pressure to the computer at the AOC.

2.2. Array

Table 2 shows the maximum lengths (B) of the KVN baselines in km and the corresponding resolutions ($\theta_{\rm HPBW}$) in milliarcseconds (mas), which is estimated as $\theta_{\rm HPBW} \sim 206.3 \times \lambda$[mm]/B[km] mas. Figure 2 shows uv-coverages for four sources with very different declinations: $-30°$, $0°$, $+30°$, $+60°$.

2.3. Baseline and image sensitivities

Table 3 shows nominal frequency ranges of KVN receivers at K- and Q-band in column (2), typical a priori System Equivalent Flux Density (SEFD) at zenith in column (3), antenna gain at the optimal elevation in column (4), typical KVN baseline sensitivity (ΔS) in column (5) and KVN 3-baseline image sensitivity (ΔI) in column (6).

The baseline sensitivities with identical KVN antennas are estimated using the formula: $\Delta S = SEFD/[\eta_{\rm s}(2\Delta\nu\tau_{\rm ff})^{1/2}]$ Jy, for typical KVN's single polarization continuum observations assuming an aggregated recorded data rate of 1024 Mbps ($\Delta\nu$ = 256 MHz), fringe-fitting intervals ($\tau_{\rm ff}$) of 100 sec (K-band) and 60 sec (Q-band), and a 2-bit sampling ($\eta_{\rm s} = 0.88$). The a priori SEFDs are estimated for typical KVN system temperatures ($T_{\rm sys}$) of 100 K (22 GHz) and 150 K (43 GHz) at zenith, using the formula: $SEFD = 2k_{\rm B}T_{\rm sys}/A_{\rm e}$, where $k_{\rm B} = 1.380 \times 10^{-23}$Joule K^{-1} is the Boltzmann constant and $A_{\rm e}$ is an effective antenna area. The typical thermal noises ($\sigma_{\rm th}$) in a single-polarization image obtained with KVN are computed for continuum observations with an on-source integration time ($\tau_{\rm obs}$) of 8 hr, using the formula: $\sigma_{\rm th} = SEFD/[\eta_s(N(N-1)\Delta\nu\tau_{\rm obs})^{1/2}]$ Jy, where N is the number of identical antennas, assuming the antennas form a homogeneous array (the same values of $SEFD$, $\Delta\nu$, and $\tau_{\rm obs}$ for all antennas). For more practical cases that only $T_{\rm sys}$ and $A_{\rm e}$ are different for each antenna, the thermal noise in an image is expressed as (Walker 1989):

$$\sigma_{\rm th} = \frac{2k_{\rm B}}{\sqrt{\Delta\nu\tau_{\rm obs}}} \frac{1}{\sqrt{(\sum_i \frac{A_{{\rm e},i}}{T_{{\rm sys},i}})^2 - \sum_i (\frac{A_{{\rm e},i}}{T_{{\rm sys},i}})^2}}, \quad (1)$$

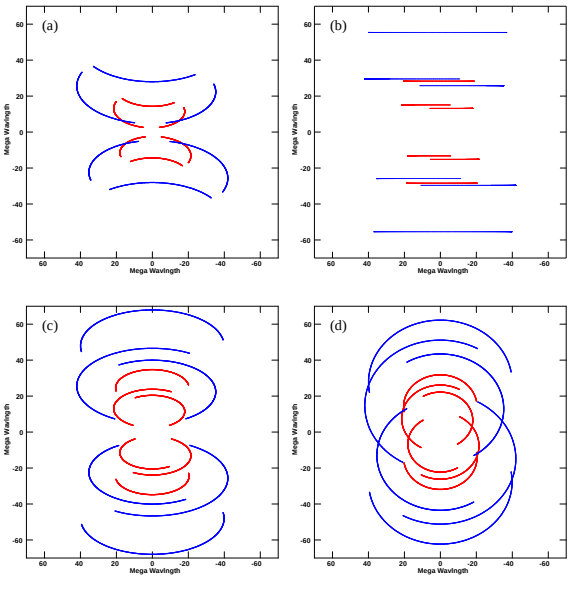

Fig. 2.— Simulated uv-coverages of KVN at K-band (red) and Q-band (blue) for sources with different declinations of (a) $-30°$, (b) $0°$, (c) $+30°$, and (d) $+60°$ for an observing time of 12 hr.

Table 1
Geographic locations of KVN stations

Location	North Longitude (o : ′ : ″)	East Latitude (o : ′ : ″)	Elevation (m)	X (m)	Y (m)	Z (m)	Code
Seoul	126:56:27.6	37:33:54.6	121.7	-3042280.9137	4045902.7164	3867374.3544	KY
Ulsan	129:14:59.1	35:32:44.2	161.4	-3287268.6186	4023450.1799	3687380.0198	KU
Jeju	126:27:34.5	33:17:20.4	441.3	-3171731.5580	4292678.4878	3481038.7252	KT

Table 2
Maximum VLBI baseline lengths and angular resolutions

Baseline	Baseline lengths (km)	Angular resolution (mas)	
		22 GHz	43 GHz
KY-KU	305	9.1	4.7
KU-KT	358	7.8	4.0
KT-KY	476	5.8	3.0

where $A_{e,i}$ and $T_{sys,i}$ are A_e and T_{sys} for antenna i.

2.4. Clock system

For VLBI observations, it is important to know the accurate time of every VLBI data sample, according to some stable station clock. The time keeping at KVN stations is conducted by clock systems consisting of four elements: a highly stable hydrogen maser, a GPS receiver, a standard clock system, and a time comparator. The hydrogen maser is to maintain time at the microsecond level with the help of one second pulse (1pps), generated from pure 5 MHz tone. The GPS receiver is used for receiving 1 pps signal from GPS satellites. At all KVN sites, two GPS receivers are installed at the backside of the subreflector and on the station control building. The GPS receiver on the building is used for the time keeping. The standard clock system is used to synchronize the 1pps signals from the hydrogen maser with those from the GPS receiver. The time comparator is to monitor any offsets between the two 1pps signals to the level of 100 nanoseconds.

The frequency stability achieved by the clock system is measured to be $\leq 2 \times 10^{-13}$ and $\leq 3 \times 10^{-15}$ (Allan deviation) at time periods of 1 s and 10^3 s, respectively.

2.5. Recording system

The KVN's VLBI data are recorded onto the magnetic disk modules at a maximum rate of 1 Gbps by the Mark 5B (Mk5B) recorder units at the stations. The recorded data are shipped via magnetic disk modules to the Mk5B playback units at the correlator. The Mk5B recording system was developed by Haystack observatory. Each Mk5B unit lodges two removable disk modules each of which consists of 8 disk drives. Disk modules of 24-TB, 16-TB, 8-TB, and 4-TB capacity are used for KVN observations.

In addition to the Mk5B system, the tape-based recording system, comprising a DIR-1000 tape recorder and a DMS-24 tape library, is equipped at each KVN station. These recording systems have been provided by National Astronomical Observatory of Japan (NAOJ) for performance test observations and scientific demonstration observations with the KVN-VERA combined network. Data rate of this recording system is 128 Mbps. The data recorded with DIR-1000 are correlated at Mitaka correlation center of the NAOJ.

2.6. Correlators

2.6.1. Daejeon Correlator

Figure 3 shows the Daejeon hardware correlator in Korea-Japan Correlation Center (KJCC).

Table 3

Baseline and image sensitivities

Frequency Band (1)	Frequency Range (GHz) (2)	SEFD (Jy) (3)	Gain (K Jy^{-1}) (4)	ΔS (mJy) (5)	σ_{th} (mJy $beam^{-1}$) (6)
K	21.25-23.25	1265	0.079	6.3	0.2
Q	42.11-44.11	1898	0.079	12	0.3

Note.—Column designation: 1 - frequency band designation; 2 - nominal frequency range; 3 - typical KVN system-equivalent-flux-density at zenith; 4 - antenna gain at the optimal elevation; 5 - typical KVN baseline sensitivity for the aggregated recorded data rate of 1024 Mbps, the integration time of 100 sec (K-band) and 60 sec (Q-band), and the bandwidth of 256 MHz; 6 - typical thermal noise in an image obtained with KVN for the on-source integration time of 8 hr.

Fig. 3.— Daejeon Correlator in KJCC, Korea.

There are several VLBI data playback systems which will be used in the combined VLBI network with KVN and VERA: Mark 5B, VERA2000, OCTADISK, and some kinds of optical fibre which shall be introduced in near future. Some of them have the VSI-H compatible interface (http://vlbi.org/vsi), but the others take the different interface for the data transmission. And also they have their own maximum data recording/play back rates respectively. To absorb all of these differences and in homogeneity among these existing VLBI data playback systems, the Raw VLBI Data Buffer (RVDB) was introduced, which is in fact a big data server with many large RAID disks and several kind of VLBI data interfaces. The VLBI Correlation Subsystem (VCS) shall receive the VLBI data from the RVDB system, shall calculate the correlation between the every possible pairs of data inputs with proper control parameters given from the correlator control and operation computer. The computing architecture of the Daejeon correlator is based on the Xilinx Field Programmable Gate Arrays (FPGAs). The VCS is designed that it is able to process maximum 16 stations, maximum 8192 Mbps/station, and 8192 output channels for VLBI observation data. And then VCS shall dump the correlation results into a data archive system. The data archive system, is also a kind of data server, which is used to capture the correlated data output from the VCS, to save them as a structured file system. Finally there is also the correlator control and operation software for overall system. The Daejeon correlator has a capability of VLBI data correlation for various VLBI networks: the Korean VLBI Network (KVN), the KVN-VERA combined Network, and the East Asia VLBI Network (EAVN).

2.6.2. Software correlator

In addition to the Daejeon correlator, a software correlator based on DiFX (Distributed FX; Deller et al. 2007, 2011) has been used mostly for the correlation of data from the KVN. A decent Beowulf cluster is dedicated for the software correlation. It is composed of one master node, 35 computer nodes, one FDR (fourteen data rate) infiniband switch, one 10-Gigabit network switch, and 1-Gigabit network switch. There are 32 cores in the master node and 16 cores in each computer node. The combined theoretical peak performance of the master and computers is 11.0 TFlop/s (Tera Floating point operations per second). A 720-Terabyte storage space is directly attached to the

master node. The FDR infiniband switch has been used for communication among master and computer nodes, and NFS (Network File System) betwen the master and computer nodes. The 10-Gigabit switch has been used for connecting three Mark 5Bs and the master server. The one-Gigabit switch has been used for the management of the cluster. The cluster has been managed using Rocks, open-source toolkit for real and virtual clusters (http://www.rocksclusters.org). The software version of DiFX has been upgraded and the current version is 2.3. There are three Mark 5Bs for the copy of scans in disk packs to the file server. All of them are connected with the 10 Gigabit network switch. There is a Mark 5B in each site of the KVN. So three Mark 5Bs in KVN stations are all connected to a dedicated one-Gigabit network.

The software correlator is very useful for fringe tests before VLBI observations. We transfer a scan recorded in Mark 5B in each site to the file server through the dedicated one Gigabit Ethernet. We then correlate the data streams from three KVN stations, perform fringe search and evaluate system health. We are planning to do routinely e-VLBI observations for fringe tests by making fully use of the one Gigabit networks.

There are four steps in the procedure for correlation of scans from three KVN stations. First, disk packs from each station are delivered to the KJCC. Second, we extract data from requested scans in each disk pack by using utility FUSE (http://fuse.sourceforge.net) and then transfer them to the file server through the 10 Gigabit network at a rate of 3.8Gbit/sec. Third, we adjust a clock offset and a rate of each station by searching fringes of first and last scans, which are usually streams from calibrators. In order to find values of clock offset and rate, we use FOURFIT, which is a fringe fitting program in the Haystack Observatory Post processing System (HOPS; http://www.haystack.mit.edu/tech/vlbi/hops.html). Finally we do correlation of all scans using DiFX. Correlator output is written according to the FITS interface Data Interchange Convention (Greisen 2009).

3. Test observations and data analysis

3.1. Observations

We conducted two test observations for evaluating VLBI performance of KVN at 22 and 43 GHz. The first observation (k10273b in Table 4) was conducted at 22 GHz on 2010 October 1 in order to confirm that the full cycle of VLBI observations works according to specification: scheduling, antenna control system, data recording, correlation, post-correlation data processing, astrometry, and geodesy. We observed four Active Galactic Nuclei (AGN): NRAO 150, OJ 287, 0838+133, and 0422+022 for 12 hours. The observing frequency band was 21.968-22.464 GHz in left-hand circular polarization (LHCP). Each source was observed with 10–13 scans of 10 min long. With the observing scheme, we were also able to evaluate the snapshot imaging capability towards compact radio sources at various declinations of $0° - 60°$.

The second observation (k11094a in Table 4) was conducted simultaneously at 22 and 43 GHz on 2011 April 4 in order to evaluate the dual-frequency full-track imaging capability towards a compact radio source with extended jet structures. We observed one of the bright AGN, 3C 84, with 148 scans of 2 min long for 9 hours. The observing frequency bands are 21.800-21.928 GHz and 43.600-43.728 GHz in LHCP. We measured system temperatures at 8 elevations: 18.21°, 20.17°, 22.62°, 25.77°, 30.00°, 36.03°, 45.58°, and 65.38° (so called sky tipping curve measurement) before and after the observations in order to check changes in the opacity of the atmosphere during the observations.

The observation data were digitized by samplers within antenna cabin resulting into 2-bit data streams with four quantization levels. The digitized signals were transmitted to the observing building through optical fibers by the optical transmission system (OTS). The digitized signals were processed by the digital filter bank (DFB), to be 16 sub-bands of 16 MHz wide with a frequency interval of 16 MHz, and recorded using the Mark 5B system at an aggregate recording rate of 1024 Mbps. The recorded data were shipped to the KJCC and correlated with the DiFX software correlator.

TABLE 4
LOG OF TEST OBSERVATIONS

Observation Name	Observation Date	**Temp:Humid** (°C:%)	Frequency Band (GHz)	**Optical depth**	Bit rate (Mbit s^{-1})	Frequency Channels	Sampling (bit)	Bandwidth (MHz)
k10273b	2010 Oct 1	16.5:77	21.968-22.464	0.11	1024	16	2	256
k11094a	2011 Apr 4	11.4:41	21.800-21.928	0.05	1024	8	2	128
			43.600-43.728	0.10	1024	8	2	128

3.2. Post-correlation processing

The DiFX correlator computed the spectrum of the cross-correlation function with resolution 0.125 MHz for every accumulation periods of 1 s (k11094a) and 2 s (k10173b) long. We performed further processing with using the VLBI analysis computer program $\mathcal{PIMA}$ (Petrov et al. 2011) and the NRAO Astronomical Image Processing System (AIPS). We used $\mathcal{PIMA}$ and AIPS for the observation, k10273b, and we used AIPS for k11094a.

3.2.1. Processing k10273b experiment with $\mathcal{PIMA}$

We split the 10 min long scans into shorter solution intervals of 200 s long. Within each solution interval we evaluated phase delay rate and group delay using all visibilities following the so-called baseline fringe search procedure described in detail in Petrov et al. (2011). The group delay τ_g and phase delay rate $\dot\tau_p$ determined with this procedure after being applied to the cross-spectrum c_{ij} provides the maximum to the coherent sum of spectrum components $C(\dot\tau_p, \tau_g)$:

$$C(\dot\tau_p, \tau_g) = \sum_{kj} c_{kj}\, w_{kj} e^{-2\pi\, i\ (\omega_o\tau_p + (t_k - t_o)\dot\tau_p + (\omega_j - \omega_o)\tau_g)}$$

where w_{kj} is weight that is a fraction of the number of correlated bits to the number of recorded bits, ω_j is the angular frequency, t_k is time since the fringe reference epoch t_o, ω_o is the reference frequency, and τ_p is phase delay. An example of the two-dimensional plot of dependency of $|C|$ on phase delay rate and group delay near the maximum is shown in Figure 4. The residuals averaged over time as a function of frequency are shown in Figure 5. The residuals averaged over frequency as a function of time are shown in Figure 6. Both plots demonstrate good health of the system.

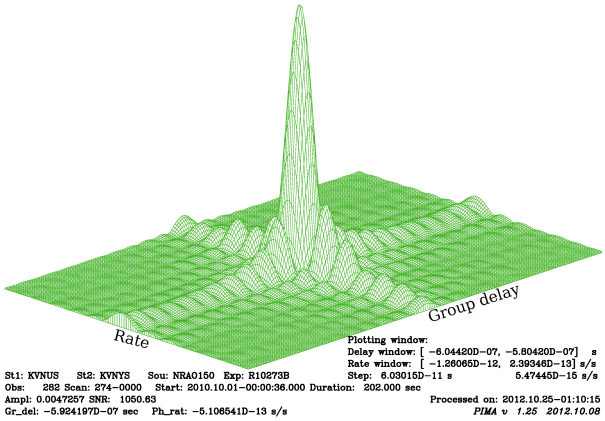

Fig. 4.— An example of the dependence of the amplitude of averaged visibilities on phase delay rate and group delay for NRAO 150 with the baseline of KY-KU at 22 GHz (k10273b). Signal-to-noise ratio of the maximum amplitude is 1051. Duration of the scan is 202 s.

3.2.2. Processing k11094a experiment with AIPS

A standard AIPS procedure was applied for post-correlation processing of k11094a. We made an antenna-based fringe fit to the multi-frequency data using AIPS task FRING. KVN Ulsan (KU) was chosen as the reference antenna. We split the 2 min long scans into shorter solution intervals of 30 s long which is corresponds to a canonical coherence time at 43 GHz. Phase delays and delay rates of each baselines were searched for individual frequency channels at 22 and 43 GHz. The baseline-based fringe solutions were used to find the antenna-based fringe solutions. The residuals averaged over time as a function of frequency are shown in Figure 7.

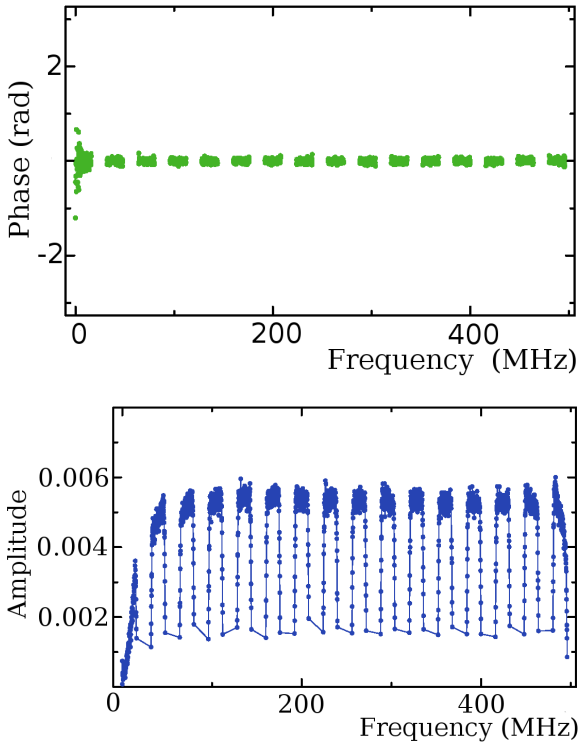

Fig. 5.— Residual phase and amplitude averaged over time for k10273b.

3.3. Amplitude calibration

Once the residual delay and rates for visibility phases were corrected, we performed the amplitude calibration. System temperatures in Kelvin ($T_{\rm sys}$) were measured during observations at KVN stations once every user-specified interval (default 10 sec) in order to calibrate amplitude variation in time due mainly to atmospheric fluctuation. The chopper-wheel method (Ulich & Haas 1976) is used for measuring $T_{\rm sys}$ at KVN antennas. According to the method, we used two loads of known temperature over the antenna horn: an ambient absorber as one hot load and the cold sky as another load. The sky tipping curve analysis is used to estimate the equivalent temperature of the cold sky (Mangum 2000). The measured $T_{\rm sys}$ is a sum of three temperatures: the receiver temperature, the spillover temperature, and the contribution of the atmosphere as described in Petrov et al. (2012). These $T_{\rm sys}$ values can be converted to SEFD by dividing by the KVN antenna gains in K Jy^{-1}. The typical values of SEFD for KVN

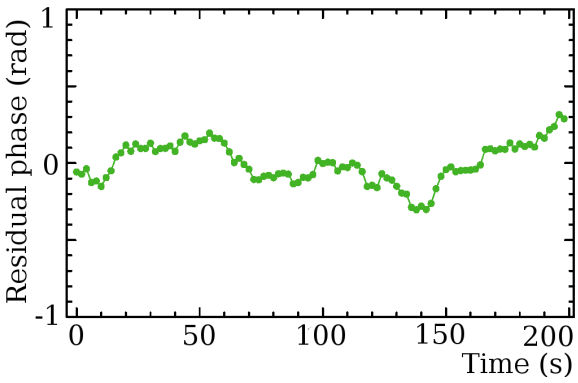

Fig. 6.— Residual phase averaged over frequency for k10273b.

antennas are summarized in Table 3. The elevation dependence of the antenna gains is also corrected based on the normalized gain curves with lease-squared-fitted second-order polynomials as derived in Lee et al. (2011).

Additional amplitude correction for the atmospheric opacity above an antenna is performed by conducting the sky tipping curve analysis. In practice, the system temperatures ($T^*_{\rm sys}$) corrected for the atmospheric opacity are estimated based on the sky tipping curve measurements once every user-specified interval (default before and after an experiment).

The fringe amplitudes were re-normalized to restore amplitude distortion due to quantization, including effects of deviation of the formatter voltage thresholds from their nominal levels.

In order to confirm the amplitude calibration with KVN, we compared the correlated flux densities of compact radio sources, OJ 287 and NRAO 150 for k10273b with those obtained from a VLBA 22 GHz observation on 2010 October 2. From the VLBA observation, we selected *uv*-data with *uv*-distances corresponding to those of the *uv*-data for each KVN baseline. Amplitudes of the *uv*-data were averaged to be compared with the mean amplitude of KVN. Ratio of the mean amplitudes $R_{ij} = F_{ij,\rm KVN}/F_{ij,\rm VLBA}$ of the baseline ij consists of amplitude correction factors $C_{i,j}$ of two antennae, i, j as $R_{ij} = 1/\sqrt{C_i C_j}$. For a VLBI network with three antennae, the correction factors are easily estimated as $C_i = R_{jk}/R_{ij}R_{ki}$. We summarized the estimated amplitude correction factors of KVN in Table 5. The maximum

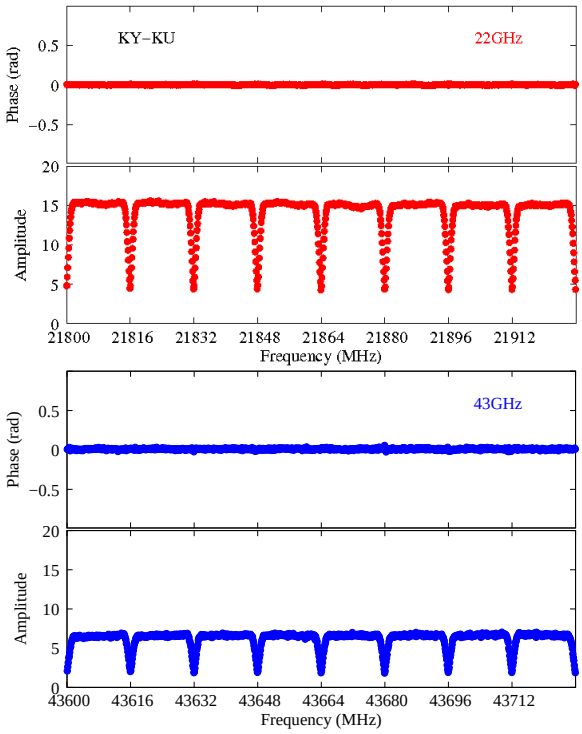

Fig. 7.— Residual phase and amplitude averaged over time for k11094a.

amplitude correction factor of KVN antennas at 22 GHz is about 13%. At 43 GHz, we found that the amplitude correction factors of KVN antennas are within 30% with using fringe search observations as described in Petrov et al. (2012). These values do not represent the rms residual errors of calibrated images, to which the image dynamic range is attributed. However, we can estimate the rms residual errors based on the standard deviation of the amplitude correction factors at three baselines. The estimated amplitude rms residual errors after calibration are less than 3% for 22 GHz and about 5% at 43 GHz.

3.4. Imaging with calibrated data

After the phase- and amplitude-calibration, the contour maps of four target sources were made using the Caltech DIFMAP software (Shepherd et al. 1994). The calibrated data are averaged in frequency within each IF. When averaging in frequency, the data at band edges are excluded, due to bandpass shape of each IF. The *uv*-data were averaged also in time over 30 seconds. After investigating the frequency- and time-averaged visibility amplitudes, some deviant data points were flagged.

The *uv*-data were then fitted with a simple Gaussian model. First, a single circular Gaussian component was applied to fit the data. Self-calibration for visibility phase and CLEAN deconvolution were applied to produce final contour maps of the detected sources. We did not modify the visibility amplitudes.

In order to evaluate the quality of the final image, we have investigated the residual noise in the image. The noise in the final image can be expressed quantitatively by the ratio of image noise rms to its mathematical expectation, ξ_r. Suppose that a residual image has an rms $\sigma_{\rm r}$ and the maximum absolute flux density $|s_{\rm r}|$. For Gaussian noise with a zero mean, the expectation of $s_{\rm r}$ is

$$|s_{\rm r,exp}| = \sigma_{\rm r}\left[\sqrt{2}\ln\left(\frac{N_{\rm pix}}{\sqrt{2\pi}\sigma_{\rm r}}\right)\right]^{1/2}, \qquad (2)$$

where $N_{\rm pix}$ is the total number of pixels in the image. The ratio ξ_r is given by

$$\xi_{\rm r} = s_{\rm r}/s_{\rm r,exp}. \qquad (3)$$

When the residual noise approaches Gaussian noise, $\xi_{\rm r} \to 1$. If $\xi_{\rm r} > 1$, not all the structure has been adequately recovered; if $\xi_{\rm r} < 1$, the image model has an excessively large number of degrees of freedom (Lobanov et al. 2006). The values of $\xi_{\rm r}$ of the images are in a range of 0.66-1.16 as presented in Table 9, implying that the images adequately represent the structure detected in the visibility data.

4. Results

4.1. Baseline length estimation

After the post-correlation processing of k10273b with $\mathcal{PIMA}$, we exported group delays determined with the fringe search procedure to VLBI analysis astrometry/geodesy software VTD/PostSolve[1]. Although the experiment was not optimized for geodesy, we are in a position to adjust baseline lengths, clock function and correction to the a priori atmosphere path delay in zenith direction. Two latter parameters were modeled with

[1]http://astrogeo.org/vtd

Table 5
Amplitude correction factors of KVN

Observation (1)	Source (2)	Band (3)	KY (4)	KU (5)	KT (6)	KY-KU (7)	KU-KT (8)	KT-KY (9)	MEAN (10)	STD (11)
k10274b	NRAO 150	K	1.117	1.035	0.980	1.075	1.007	1.046	1.043	0.028
	OJ 287	K	1.011	1.080	1.131	1.045	1.105	1.069	1.073	0.025
QCAL1	calibrators	Q	1.10	1.06	1.31	1.080	1.178	1.200	1.153	0.052

Note.—Column designation: 1 - observation name, QCAL1 from Petrov et al. (2012); 2 - source name; 3 - frequency band; 4-6 - amplitude correction factors for antennas; 7-9 - amplitude correction factors for baselines; 10,11 - mean and standard deviation of 7-9.

B-spline with a time step of 60 minutes. Since VLBI path delay is invariant to a rotation and translation of the coordinate system, the analysis of VLBI data themselves does not allow us to determine a unique set of station coordinates, but only to determine a family of solutions with 6 arbitrary parameters. In a case of analysis of a network of three stations not connected with other networks, this arbitrariness in a choice of 6 free parameters makes such estimates of station positions meaningless. Therefore, we restrict our analysis of baseline lengths.

Figure 8 shows postfit residuals at baseline KT/KU. The residuals do not exhibit systematic patterns. The weighted root mean square (wrms) of residuals is 14.8 ps. This is below the typical wrms of postfit residuals 20–40 ps in regular geodetic VLBI observations under the International VLBI Service for Geodesy (IVS) observing programs. Table 6 shows baseline lengths determined from k10273b experiment. The quoted uncertainties are formal errors computed according to the error propagation law from group delay uncertainties. Formal uncertainties 2–4 mm over 12 hour observations are rather small comparing to 2–10 mm typical baseline lengths errors in 24 h IVS geodetic observing sessions. The presented baseline length results should be taken cautiously. Observing only four sources instead of 50–100 in a typical geodetic experiment may introduce noticeable systematic errors. Analysis of baseline length systematic errors is beyond the scope of the present paper.

4.2. Coherence time

Scans of 10 min long of k10273b may exceed the limit set by instability of the frequency standards

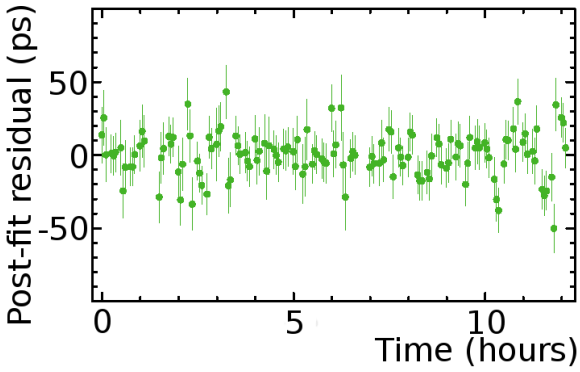

Fig. 8.— Group Delay Post-fit Residuals at Baseline KT/KU.

and variations in the path delay through the neutral atmosphere. The signal to noise ratio (SNR) is scaled as a square root of the integration time in the case of a perfect observing system and absence of coherency losses due to fluctuations of the path length through the atmosphere. The deviation from the square root law defined as $\mathrm{SNR} = D\sqrt{t_{\mathrm{int}}}$ we call a decorrelation factor. Decorrelation factor is a number between 1.0 and 0.0 which scales the SNR. Factor 1.0 means no decorrelation and factor 0.0 means complete decorrelation. In order to investigate decorrelation at long solution intervals, we ran 10 trial solutions with using only a first portion of data of each scan 60 s, 120 s, 180 s, ... 600 s long, with remaining data being discarded. Then for each scan the SNR at a solution interval t was divided by the SNR at the shortest solution interval, $t_o = 60$ s, and by $\sqrt{t/t_o}$, which gave as decorrelation factors. The decorrelation factors averaged over entire experiment are shown in Figure 9. We see that the decorrelation is still not high even at 600 s long scans. For instance, an

Table 6

Baseline Lengths Determined from K10273B VLBI Experiment and their Uncertainties.

Baseline	Baseline length (m)
KT-KU	358342.5615 ± 0.0038
KT-KY	476351.7053 ± 0.0049
KU-KY	304829.5071 ± 0.0024

increase of integration time from 300 s to 600 s improves the SNR by a factor 1.30. This is less than $\sqrt{2} = 1.41$ that we would have had in the absence of decorrelation, but still a noticeable increase. We conclude that (1) decorrelation due to instability in the hardware at times up to 600 s is negligible; (2) the atmosphere fluctuations at KVN baseline are partly coherent, which allows us to extend integration time under good weather conditions up to 600 s without significant loss of coherence. Taking into the decorrelation factors and the typcial SEFD used for Table 3, we summarized the detection limit (SNR=6) at K-band for several integration times in Table 7.

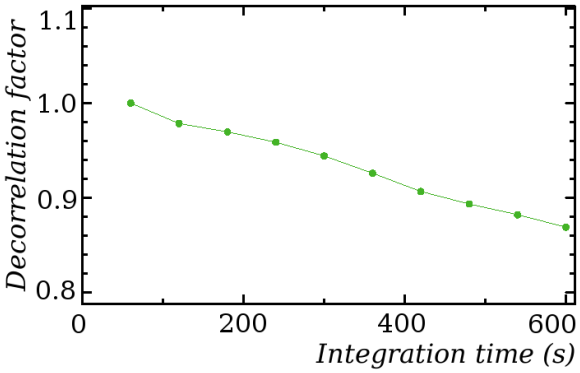

Fig. 9.— **The average decorrelation factors as a function of integration time for k10273b (22 GHz) observations at KVN baselines.**

4.3. Measured sensitivity

In order to verify the estimates of the a priori SEFDs of KVN antennas, (see section 2.3), we **measured baseline sensitivity ΔS_{ij} and** determined a posteriori SEFD ($SEFD_{\rm m}$) from the observations k10273b at 22 GHz band. From the first principles of the baseline sensitivity of antennas i, j: $\Delta S_{ij} = \sqrt{SEFD_i SEFD_j}/[\eta_{\rm s}(2\Delta\nu\tau_{\rm ff})^{1/2}]$ Jy, one can caculate the a posteriori SEFD, $SEFD_{{\rm m},i}$, for one of three antennas using their measured baseline sensitivities, $\Delta S_{{\rm m},ij}$, $\Delta S_{{\rm m},jk}$, $\Delta S_{{\rm m},ki}$ as $SEFD_{{\rm m},i} = C\Delta S_{{\rm m},ij}\Delta S_{{\rm m},ki}/\Delta S_{{\rm m},jk}$, where $C = \eta_{\rm s}(\Delta\nu\tau_{\rm ff})^{1/2}$. For a scan of 10 min long of k10273b for the baseline between KT and KU, a standard deviation of visibility amplitudes accumulated at a time interval of $\tau_{\rm ff}$=2 sec does represent the baseline sensitivity, $\Delta S_{\rm KT-KU}$, at 2 sec for the baseline. We obtained the baseline sensitivities for an effective bandwidth of 14.4 MHz by averaging those for 14 sub-bands (exculding the first and last sub-bands) with the effecive bandwidth, **as summarized in Table 8.** For the scan, we compared the a priori SEFDs with the a posteriori SEFD derived from the measured baseline sensitivities. The ratios of $SEFD_{{\rm m},i}/SEFD_i$ have been averaged for all scans resulting in 1.02, 1.19, and 1.05 for KY, KU, and KT, respectively. **The ratios may be considered as the upper limit of uncertainties of antenna gain measurements since there also be the uncertainties of the system efficiency factor $\eta_{\rm s}$ which accounts for various losses in the electronics and digital equipment. The uncetainties may be attributed to uncertain assessment of quantization losses, non-square bandpasses, polarization impurity, etc (Walker 1995).**

4.4. Imaging capability

Calibrated visibility data enable us to recover the sky distribution of the observed compact radio sources even for three-element VLBI networks such as KVN. Although we are not in a position to make use of amplitude self-calibration technique which is of great benefit to the VLBI imaging, we are able to conduct a reliable imaging with using phase self-calibration and the a priori amplitude calibration as described in section 3.4.

In Figure 10 and Figure 11, we present CLEANed images for each source of two observations,

Table 7

Detection limits at K-band taking into account decorrelation factors

Int. time (sec)	D	$\Delta S^{SNR=6}_{SEFD=1222}$ (mJy)	$\Delta S^{SNR=6}_{SEFD=3322}$ (mJy)
60	1.00	51.1	139.0
120	0.99	36.7	99.7
240	0.96	26.7	72.7
600	0.87	18.6	50.5

Note.—For the estimation, we used the best and worst SEFDs of 1222 and 3322, and the effective bandwidth of 221.25 MHz from Table 10.

Table 8

Baseline sensitivities

Observation (1)	Name (2)	Band (3)	$BW_{\rm eff}$ (4)	$\Delta S_{\rm m,2sec}(\Delta S_{\rm m}/\Delta S_{\rm e})$ KY-KU (5)	KU-KT (6)	KT-KY (7)
k10274b	NRAO 150	K	14.4	290 (1.02)	309 (1.02)	234 (1.00)
	OJ 287	K	14.4	340 (1.27)	386 (1.31)	293 (1.16)
	0838+066	K	14.4	309 (1.11)	317 (1.04)	238 (0.93)
	0422+022	K	14.4	281 (0.94)	297 (0.95)	236 (0.96)

Note.—Column designation: 1 - observation name; 2 - source name; 3 - frequency band; 4 - effective bandwidth [MHz] used for measurement and estimation of baseline sensitivities; 5-7 - measured baseline sensitivity at integration time of 2 sec [mJy] with averaged ratio of the measured baseline sensitivity to estimated baseline sensitivity in parentheses.

Table 9

Image parameters

Observation (1)	Name (2)	α_{2000} (3)	δ_{2000} (4)	Band (5)	$B_{\rm maj}$ (6)	$B_{\rm min}$ (7)	$B_{\rm PA}$ (8)	$S_{\rm p}$ (9)	$\sigma_{\rm m}$ (10)	D (11)	$\xi_{\rm r}$ (12)
k10274b	NRAO 150	03 59 29.747	+50 57 50.162	K	5.43	3.15	81.3	8714	27.4	318	0.69
	OJ 287	08 54 48.875	+20 06 30.641	K	5.19	3.09	88.0	3380	7.69	420	0.66
	0838+066	08 40 47.588	+13 12 23.564	K	5.22	3.13	86.2	1100	3.46	317	0.97
	0422+022	04 22 52.215	+02 19 26.932	K	6.08	3.13	-79.2	668	1.92	347	0.97
k11094a	3C 84	03 19 48.160	+41 30 42.104	K	5.28	3.50	89.8	15074	12.4	1221	1.16
	3C 84	03 19 48.160	+41 30 42.104	Q	3.10	1.33	-83.3	6014	6.72	894	1.06

Note.—Column designation: 1 - Observation name; 2 - source name; 3,4 - source coordinates; 5 - frequency band; 6-8 - restoring beam: 6 - major axis [mas]; 7 - minor axis [mas]; 8 - position angle of the major axis [°]; 9 - peak flux density [mJy beam^{-1}]; 10 - off-source RMS in the image [mJy beam^{-1}]; 11 - Dynamic range of the image ($D = S_{\rm p}/\sigma_{\rm m}$); 12 - quality of the residual noise in the image.

Table 10

Image sensitivities

Observation (1)	Name (2)	Band (3)	$BW_{\rm eff}$ (4)	$T_{\rm obs}$ (5)	$N_{\rm scan}$ (6)	$SEFD$(KY:KU:KT) (7)	$\sigma_{\rm th}$ (8)	$\sigma_{\rm m}$ (9)	R (10)	$\Delta\phi$ (11)	ϵ (12)
k10274b	NRAO 150	K	221.25	120	12	1503 : 2923 : 1772	1.03	27.4	26.6	<1.5	<2.7
	OJ 287	K	221.25	120	12	1568 : 2657 : 2215	1.01	7.69	7.6	<1.2	<2.0
	0838+066	K	221.25	100	13	1568 : 2657 : 2025	0.97	3.46	3.6	<1.6	<2.8
	0422+022	K	221.25	100	10	1568 : 3322 : 1772	1.23	1.92	1.5	<1.3	<2.2
k11094a	3C 84	K	128.00	324	148	1222 : 1289 : 1329	0.49	12.4	25.3	<1.4	<2.4
	3C 84	Q	128.00	324	148	2462 : 1748 : 2259	0.82	6.72	8.2	<1.9	<3.3

Note.—Column designation: 1 - observation name; 2 - source name; 3 - frequency band; 4 - effective bandwidth [MHz] used for the image; 5 - integration time [min]; 6 - Number of observing scans for the image; 7 - System Equivalent Flux Density [Jy]: KY - KVN Yonsei: KU - KVN Ulsan: KT - KVN Tamna; 8 - estimated thermal noise in the image [mJy]; 9 - off-source RMS in the image [mJy beam^{-1}]; 10 - Ratio of the thermal noise to the off-source RMS; 11 - residual phase error [°]; 12 - amplitude rms residual error [%].

k10273b and k11094a, respectively. In the left panel, the contour map of each source is shown, with the X- and Y-axis in the units of milliarcseconds. For each source, the source name and the observation date are given in the upper left corner of the map. The lowest contour level is identified in the lower right corner of the map. The shaded ellipse represents the FWHM of the restoring beam in the image. In all of the images, the contours have a logarithmic spacing and they are drawn at -1, 1, 1.4,...,1.4^n of the lowest flux density level. In the middle panel, the plot of the visibility amplitudes against uv-radius is shown. The corresponding uv-sampling distribution is given in the inset. The X-axis of the plot of the visibility amplitude represents the uv-radius which is the length of the baseline used to obtain the corresponding visibility point. The uv-radius is given in the units of $10^6\lambda$, where λ is the observing wavelength. The Y-axis of the plot shows the amplitude of each visibility point (i.e., correlated flux density) in units of Jy. The uv-sampling distribution in the inset of the left panel describes the overall distribution of the visibility in the uv-plane, whose maximum scale equals that of the uv-radius. In the right panel, the distribution of residual noise within a residual image is shown with a Gaussian fit to the distribution. The quality of the final images were investigated a) by confirming that the distributions of residual noise were well fitted to a Gaussian distribution, and b) by qualitatively estimating the quality of the residual noise, q, as described in Section 3.4 and summarized in Table 9. Based on the VLBA images at 15 GHz (Lister et al. 2009), we confirmed that the core-dominated compact structures of four target sources, NRAO 150, OJ 287, 0838+133, and 0422+022 are well recovered with the snapshot observations with KVN. The image of 3C 84 at 22 GHz shows the prominent lobe-dominated structures at North and South about 10 mas away from the core component in the image center. The imaged structures are reliably confirmed by VLBI images from previous observations at other VLBI networks (Vermeulen et al. 1994; Walker et al. 2000; Lister et al. 2009). At 43 GHz, the KVN image shows only a core-dominated structure within a few mas, which corresponds to the previous VLBI images (Dhawan et al. 1998; Nagai et al. 2012; Suzuki et al. 2012). This may imply that the lobe structures have steep spectrum between 22 and 43 GHz, so that they are weaker than ∼7 mJy, the lowest brightness level found at existing images.

More detailed parameters of the images presented in Figure 10 and 11 are summarized in Table 9. For each image, Table 9 lists the source name, the parameters of the restoring beam (the size of the major axis, $B_{\rm maj}$ and the minor axis, $B_{\rm min}$, and the position angle of the beam, $B_{\rm PA}$), the peak flux density, $S_{\rm p}$, the off-source RMS, σ, the dynamic range of the image, and the quality of the residual noise in the image.

With these imaging results, we confirmed that KVN observations both in snapshot and and full-

track modes enable us to precisely recover the structures of compact radio sources at angular resolutions of $10-35$ Mλ and $20-70$ Mλ for wavelengths of 13 and 7 mm, respectively.

4.5. Dynamic range and residual errors

Dynamic range attained on an image is widely defined as the ratio between the peak brightness on the image and the residual noise in the off-source regions. Since the distribution of the residual noise in the image behaves somewhat like the side lobes in the beam and these side lobes are almost always greatest near the peak, the noise will be greater in regions containing source structures. However, the noise in a blank region of an image made with sufficiently well-calibrated data adequately covering the uv-plane will be a good indicator of true error in the image. Therefore, the dynamic range defined above will be a good indicator of image fidelity (Perley 1999).

We found that the dynamic range achieved with the KVN images for k10274b is within 317-420 for the sources with various peak flux densities of 0.67-8.7 Jy/beam (see column (11) in Table 9). This implies that the residual noise levels of the images (imaging sensitivities) are different for each target source, and most likely higher than the thermal noise of each image (see columns (8)-(10) in Table 10).

The higher residual noise than the thermal noise may be due mainly to 1) the effect of incomplete *uv*-coverage and 2) the effect of residual calibration errors (Perley 1999). The first effect could also be described as instabilities or inaccuracies in the deconvolution process, since in the case of complete *uv*-coverage, no deconvolution is necessary and therefore no such instabilities or inaccuracies will occur. This effect is largely confined to the regions where the source structures were sought in the deconvolution process. We estimated the residual noise around the regions containing the source structures. We found that the residual noises are higher by $\leq 30\%$ than those in blanck regions. For relatively fainter sources, however, 0838+066 and 0422+022, the residual noises in the source region are similar to those in the blank regions. Therefore, we can conclude that the effect of the incomplete *uv*-coverage to the residual noise is likely small.

The second effect is due to phase and amplitude calibration errors from antenna-based or baseline-based uncertainties. Perley (1999) derives that for a single snapshot observation with N antennas a random baseline-dependent error $\Delta\phi$ for all baselines will limit the dynamic range to

$$D = \frac{\sqrt{N(N-1)}}{\Delta\phi}. \quad (4)$$

And if M successive snapshots are independent (errors are different between snapshots), then the dynamic range becomes

$$D = \frac{\sqrt{M}\sqrt{N(N-1)}}{\Delta\phi}. \quad (5)$$

Since we measured the dynamic ranges with the images, we applied the equation (5) to our results for estimating the residual baseline-dependent phase errors assuming that the errors are independent between scans; $M = 10-13$ for k10274b and $M = 148$ for k11094a. We assume here that the phase errors are not independent within a scan although the scan length exceeds a coherence time. We find the residual baseline-dependent phase errors are 1.2-1.6 degrees at 22 GHz, and 1.9 degrees at 43 GHz, respectively. It should be noted that the baseline-dependent phase errors are the residuals after phase-only self-calibration and arise mainly from baseline-based uncertainty, since the self-calibration corrects only for antenna-based errors. Perley (1999) also gives estimates for the effect of amplitude rms residual errors, ϵ, on the dynamic range as

$$D = \frac{\sqrt{M}\sqrt{N(N-1)}}{\epsilon}. \quad (6)$$

With the similar estimates as for residual baseline-dependent phase errors, we find the amplitude residual errors are 2.0%-2.7% at 22 GHz, and 3.3% at 43 GHz, respectively. These values are consistent with the estimates of the amplitude rms residual errors obtained in section 3.3.

The estimated phase and amplitude errors should be considered as upper limits since they are estimated under assumption that the other error or effect (such as of incomplete *uv*-coverage) is small, but not negligible. Therefore, we conclude that the KVN is ready for imaging compact radio sources both in snapshot and full-track modes

with residual baseline-dependent phase errors less than 2 degrees at 22 and 43 GHz, amplitude rms residual errors less than 5% at 22 and 43 GHz, and with dynamic ranges of 300 for snapshot mode and 1000 for full-track mode.

4.6. Spectral index map

For making spectral index maps, we should take into account three main effects. First, the effect of flux density variability and possible proper motion of jet components should be considered. We must take the observations at very close epochs or simultaneously, if possible. This effect will be negligible with KVN. Next, the angular resolution must be the same at multi-frequencies and the *uv*-coverage as similar as possible; this will provide us with the same sensitivity to extended structures in the high- and low-frequency images. We are not in a position to effectively take this effect into account with KVN, since the *uv*-coverages at each frequency are strictly fixed. However, in the general imaging process, we are able to restore the synthesized beam so that the angular resolution will match each other. Finally, as absolute position is not available, we need to properly align the images before combining them. The misalignment between the images at different frequencies could be caused mainly by the opacity-induced position shift of the VLBI core, called as *core shift* (Lobanov 1998), in a synchrotron self-absorbed jet. In a specific case of 3C 84, the core shift has not been reported either at 22-43 GHz or at lower frequencies (e.g., Pushkarev et al. 2012), due partially to its complex structure in the central region. However, we may be able to predict the upper limit of the core shift to be 0.1 mas between 22 GHz and 43 GHz according to a systematic study of the core shift (see Equation (5) and Table 2 in Kovalev et al. 2008). Taking into account the pixel size of the 43 GHz-image is 0.25 mas (one fifth of the minor beam axis), the possible core-shift effect to the spectral index map is negligible.

Taking all these effects into account, the images of 3C 84 at 22 GHz and 43 GHz are used to make a spectral index map. We restored both images with a circular beam of 3.5 mas whose size corresponds to the minor axis of the synthesized beam of the 22 GHz-images. And the re-convolved images were simply combined without any position shift to make the spectral index map, as shown in Figure 12, defining the spectral index via $S_\nu \propto \nu^\alpha$.

Figure 12 represents the first parsec scale spectral-index map of 3C 84. Since 3C 84 is core-dominated at 43 GHz, the spectral index map is shown only in the core region within ∼5 mas from the center. The core region has a flat spectrum (spectral index $-0.5 < \alpha < 0$) in the inner region, implying that multiple optically thick emission regions in the core region although a gradual steepening trend can be seen. In fact, complex core structures within a few mas have been observed by previous higher resolution VLBI studies (Vermeulen et al. 1994; Dhawan et al. 1998; Walker et al. 2000; Lister et al. 2009; Nagai et al. 2012; Suzuki et al. 2012). We conclude that KVN can be used to make parsec-scale spectral-index maps of compact radio sources with simultaneous multi-frequency observations.

5. Summary

The VLBI observing performance of the KVN has been tested with observing compact radio sources at 22 GHz and 43 GHz in a recording rate of 1 Gbps. Through the performance tests, we found:

- the full cycle of VLBI observations works properly according to specification: scheduling, antenna control system, data recording, correlation, post-correlation data processing, astrometry, geodesy, and imaging analysis.
- decorrelation due to instability in the hardware at times up to 600 s is negligible. The atmosphere fluctuations at KVN baseline are partly coherent, which allows us to extend integration time under good weather conditions up to 600 s without significant loss of coherence.
- postfit residuals at KVN baselines do not exhibit systematic patterns, and the weighted root mean square (wrms) of residuals is 14.8 ps, which is below the typical wrms of postfit residuals 20–40 ps in regular geodetic VLBI observations under the International VLBI Service for Geodesy (IVS) observing programs.

- KVN observations both in snapshot and and full-track modes enable us to precisely recover the structures of compact radio sources at angular resolutions of $10-35$ Mλ and $20-70$ Mλ for wavelengths of 13 and 7 mm, respectively.
- KVN is ready for imaging compact radio sources both in snapshot and full-track modes with residual phase calibration noises less than 2 degrees at 22 and 43 GHz and with dynamic ranges of 300 for snapshot mode and 1000 for full-track mode.
- KVN can be used to make parsec-scale spectral-index maps of compact radio sources with simultaneous multi-frequency observations.

We are grateful to all staff members and students in KVN who helped to operate the array and to correlate the data. The KVN is a facility operated by the Korea Astronomy and Space Science Institute.

REFERENCES

Deller, A., Tingay, S. J., Bailes, M., & West, C. 2007, PASJ, 119, 318

Deller, A. T., Brisken, W. F., Phillips, C. J., Morgan, J., Alef, W., Cappallo, R., Middelberg, E., Romney, H., Rottmann, H., Tingay, S. J., & Wayth, R. 2011, PASJ, 123, 275

Dhawan, V., Kellermann, K. I., & Romney, J. D. 1998, AJ, 498, L111

Greisen, E. W. 2009, AIPS Memo 114

Han, S.-T., Lee, J.-W., Kang, J., Je, D.-H., Chung, M.-H., Wi, S.-O., Sasao, T., & Wylde, R. 2008, Int. J. Infrared Milli. Waves, 29, 69

Han, S.-T., Lee, J.-W., Kang, J. et al. Oh, C.-S., Byun, D.-Y., Je, D.-H., Chung, M.-H., Wi, S.-O., Song, M., Kang, Y.-W., Lee, S.-S., Kim, S.-Y., Sasao, T., Goldsmith, P. F., & Wylde, R. 2013, PASP, 125, 539

Kim, H.-G., Han, S.-T., Sohn, B. W., Oh, S.-J., Je, D.-H., Wi, S.-O., & Song, M.-G. 2004, Proc. of the 7th EVN Symp., ed. Bachiller, R., Colomer, F., Desmurs, J.J., de Vicente, P. (eds.), 281

Kim, K.-T., Byun, D.-Y., Je, D.-H., Wi, S.-O., Bae, J.-H., Jung, T.-H., Lee, C.-H., Han, S.-T., Song, M.-G., Jung, J.-H., Chung, H.-S., & Kim, H.-R., Kim, B. G. 2011, J. Korean Astron. Soc., 44, 81

Kovalev, Y. Y., Lobanov, A. P., Pushkarev, A. B., & Zensus, J. A. 2008, A&A, 483, 759

Lee, S.-S., Byun, D.-Y., Oh, C. S., Han, S.-T., Je, D.-H., Kim, K.-T., Wi, Seog-Oh, & Cho, S.-H. 2011, PASP, 123, 1398

Linsky, J. L. 1973 ApJS, 25, 163

Lister, M. L., Aller, H. D., Aller, M. F., Cohen, M. H., Homan, D. C., Kadler, M., Kellermann, K. I., Kovalev, Y. Y., Ros, E., Savolainen, T., Zensus, J. A. & Vermeulen, R. C. 2009, AJ, 137, 3718

Lobanov, A. P. 1998, A&A, 330, 79

Lobanov, A. P., Krichbaum, T. P., Witzel, A., & Zensus, J. A. 2006, PASJ, 58, 253

Mangum, J. G. 1993 PASP, 105, 117

Mangum J. G. 2000, Users's manual for the NRAO 12 meter millimiter-wave telescope Kitt Peack, Arizona (NRAO, Tucson, Arizona),

Nagai, H., Orienti, M., Kino, M., Suzuki, K., Giovannini, G., Doi, A., Asada, K., Giroletti, M., Kataoka, J., D'Ammando, F., Inoue, M., Lähteenmäki, A., Tornikoski, M., León-Tavares, J., Kameno, S., & Bach, U. 2012, MNRAS, 423, 122

Perley, R. A. 1999, in *Synthesis Imaging in Radio Astronomy II*, eds. G. B. Taylor, C. L. Carilli, & R. A. Perley, ASP Conf. Ser., 180, 275

Petrov, L., Y. Y. Kovalev, E. B. Fomalont, & D. Gordon, 2011, AJ, 142, 35

Pushkarev, A. B., Hovatta, T., Kovalev, Y. Y., Lister, M. L., Lobanov, A. P., Savolainen, T., & Zensus, J. A. 2012, A&A, 545, 113

Petrov, L., Kovalev, Y. Y., Fomalont, E. B., & Gordon, D. 2011, AJ, 142, 35

Petrov, L., S.-S. Lee, J. Kim et al. Petrov, L., Lee, S.-S., Kim, J., Jung, T., Oh, J., Sohn, B. W., Byun, D.-Y., Chung, M.-H., Je, D.-H., Wi, S.-O., Song, M.-G., Kang, J., Han, S.-T., Lee, J.-W., Kim, B. G., Chung, H., & Kim, H.-G. 2012, AJ, 144, 150

Shepherd, M. C., Pearson, T. J., & Taylor, G. B. 1994, BAAS, 26, 987

Suzuki, K., Nagai, H., Kino, M., Kataoka, J., Asada, K., Doi, A., Inoue, M., Orienti, M., Giovannini, G., Giroletti, M., Lähteenmäki, A., Tornikoski, M., León-Tavares, J., Bach, U., Kameno, S., & Kobayashi, H. 2012, ApJ, 746, 140

Ulich, B. L., & Haas, R. W. 1976, ApJS, 30, 247

Vermeulen, R. C., Readhead, A. C. S., Backer, D. C. 2000, ApJ, 430, 41

Walker, R. C. 1989, in *Very Long Baseline Interferometry* eds. M. Felli & R. E. Spencer (Dordrecht: Kluwer), 163-182

Walker, R. C. 1995, in *Very Long Baseline Interferometry and the VLBA* eds. J. A. Zensus, P. J. Diamond, & P. J. Napier (San Francisco: ASP), 133-157

Walker, R. C., Dhawan, V., Romney, J. D., Kellermann, K. I., & Vermeulen, R. C. 2000, ApJ, 530, 233

This 2-column preprint was prepared with the AAS LaTeX macros v5.2.

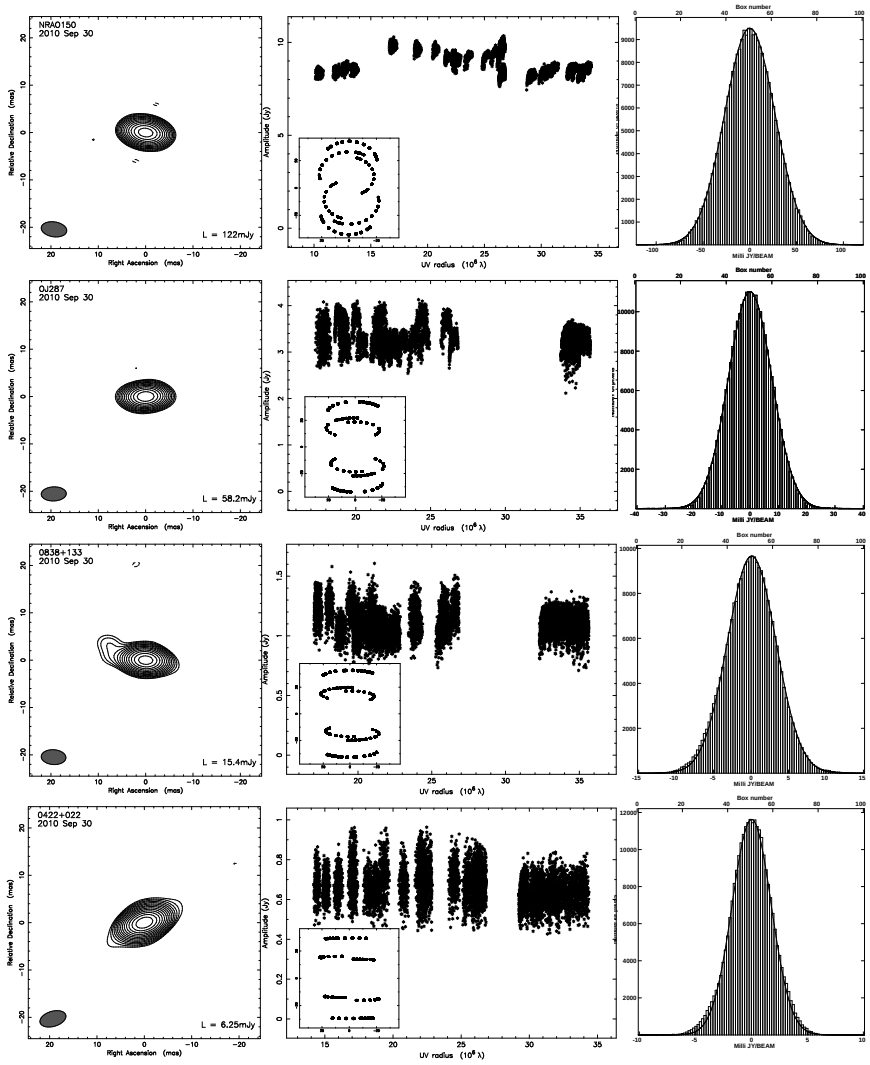

Fig. 10.— (*Left*) CLEANed images. The axes of each map are the relative RA and DEC offsets from the tracking center in milliarcseconds. The lowest contour level is shown in the lower-right corner of each map. The contours have a logarithmic spacing and are drawn at -1, 1, 1.4,...,1.4^n of the lowest contour level. (*Middle*) Distributions of the visibility amplitude against *uv*-radius and of the *uv*-sampling. The X-axis shows the *uv*-distance in $10^6\lambda$, and the Y-axis represents the visibility amplitude (correlated flux density) in Jy, averaged over 30 seconds. The corresponding *uv*-sampling distribution is given in the inset. (*Right*) The noise distribution within the image. The solid curve represents the Gaussian fit to the distribution. Image parameters of each image are summarized in Table 9.

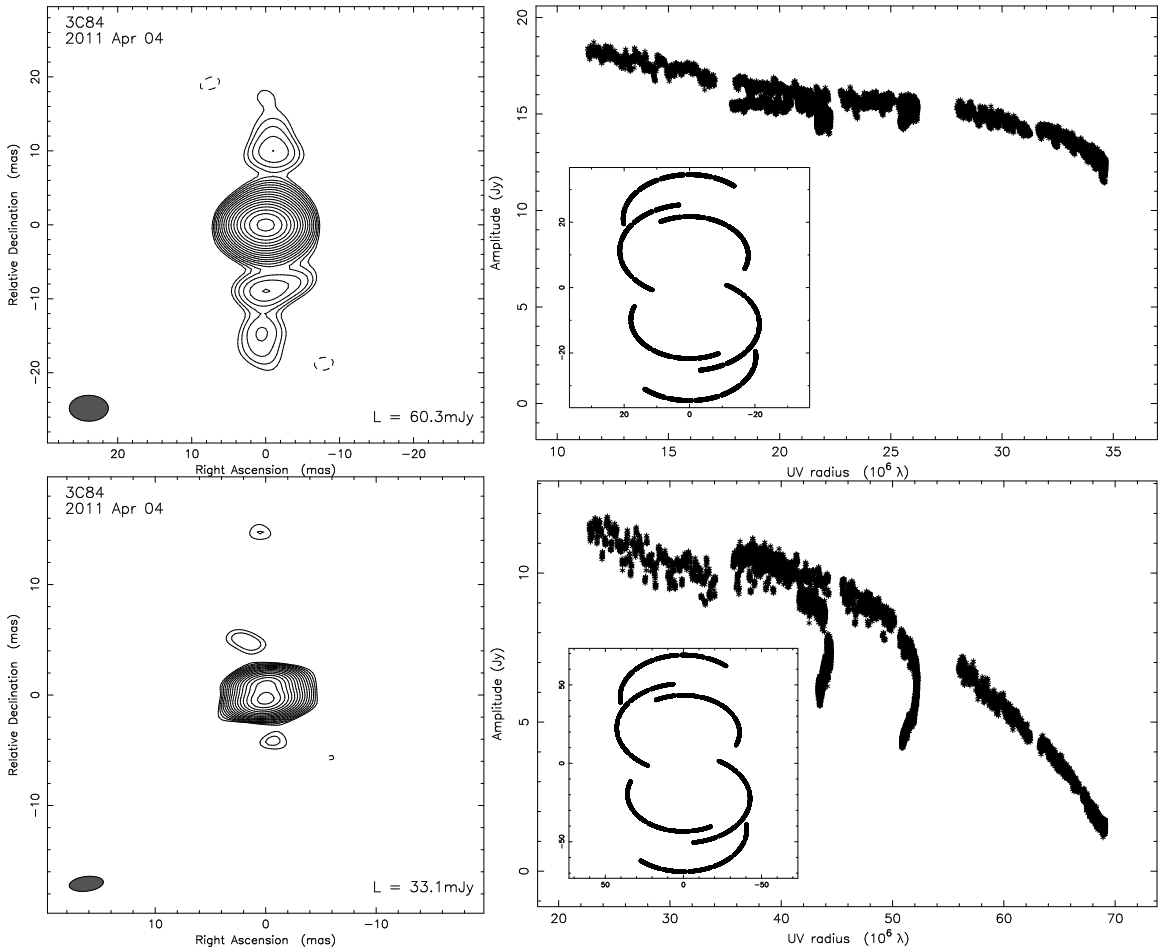

Fig. 11.— (*Left*) CLEANed images of 3C 84 simultaneously observed at 22 GHz (upper) and 43 GHz (lower). The axes of each map are the relative RA and DEC offsets from the tracking center in milliseconds. The lowest contour level is shown in the lower-right corner of each map. The contours have a logarithmic spacing and are drawn at -1, 1, 1.4,...,1.4^n of the lowest contour level. (*Right*) Distributions of the visibility amplitude against *uv*-radius and of the *uv*-sampling. The X-axis shows the *uv*-distance in $10^6\lambda$, and the Y-axis represents the visibility amplitude (correlated flux density) in Jy, averaged over 30 seconds. The corresponding *uv*-sampling distribution is given in the inset. Image parameters of each image are summarized in Table 9.

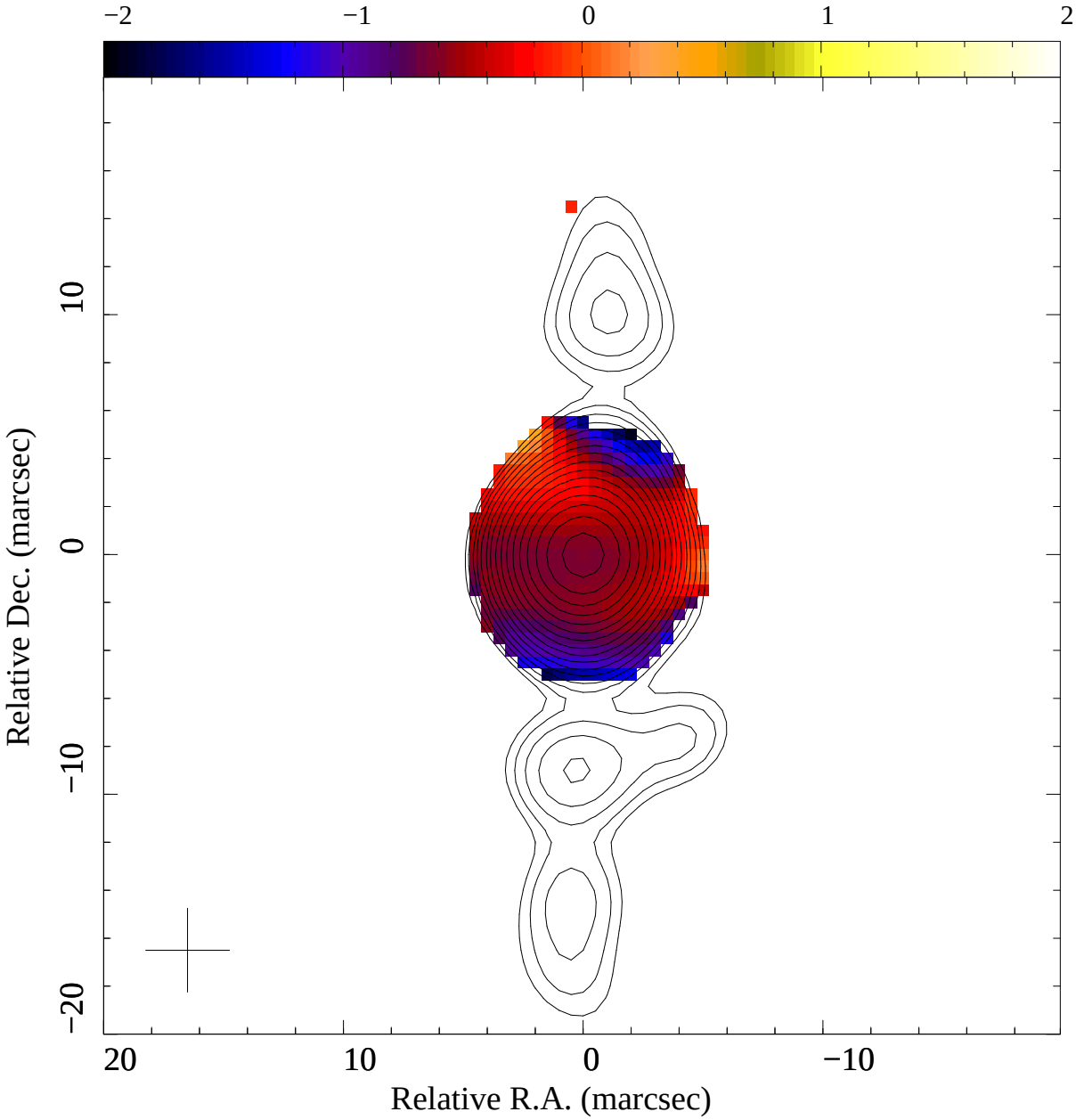

Fig. 12.— Spectral index map (color) of 3C 84 from the images at 22 GHz and 43 GHz. The CLEAN image at 22 GHz is shown in contour. Both maps are restored with a beam of 3.5×3.5 represented by the cross in the lower left corner. The axes of each map are the relative RA and DEC offsets from the tracking center in milliarcseconds.